Physics – Uspekhi **66** (2) 195 – 212 (2023)

INSTRUMENTS AND METHODS OF INVESTIGATION PACS numbers: **25.75. – q,** 29.20.db

NICA Booster: a new-generation superconducting synchrotron

A V Butenko, O I Brovko, A R Galimov, E V Gorbachev, S A Kostromin, V N Karpinsky, I N Meshkov, V A Monchinskiy, A O Sidorin, E M Syresin, G V Trubnikov, A V Tuzikov, A V Philippov, H G Khodzhibagiyan

DOI: https://doi.org/10.3367/UFNe.2021.12.039138

Contents

Abstract. In November–December 2020 and in September 2021, the first two beam runs of the Booster Synchrotron — a new cyclic accelerator of the NICA (Nuclotron-based Ion Collider fAcility) complex — were performed at the Laboratory for High Energy Physics, Joint Institute for Nuclear Research. New technologies (previously not used in Russia) were developed for the Booster's construction based on new physical and technological solutions. We describe these technologies and solutions and also the methods used in constructing and testing the accelerator systems. We present the results of the first two runs.

Keywords: ion synchrotron, superconducting magnets, ultrahigh vacuum, beam cooling

A V Butenko, O I Brovko, A R Galimov, E V Gorbachev, S A Kostromin, V N Karpinsky, I N Meshkov, V A Monchinskiy, A O Sidorin [(a)], **E M Syresin** [(b)], **G V Trubnikov, A V Tuzikov, A V Philippov, H G Khodzhibagiyan**
Joint Institute for Nuclear Research,
ul. Joliot-Curie 6, 141980 Dubna, Moscow region, Russian Federation
E-mail: [(a)] sidorin@jinr.ru, [(b)] esyresin@jinr.ru, post@jinr.ru

Received 11 August 2021, revised 2 December 2021
Uspekhi Fizicheskikh Nauk **193** (2) 206 – 225 (2023)
Translated by S Alekseev

To the blessed memory of A D Kovalenko

1. Introduction

In the late 1970s, the High Energy Laboratory (HEL) of the Joint Institute for Nuclear Research (JINR) designed a project involving a heavy-ion accelerator complex for advanced research in relativistic nuclear physics. The complex included the Nuclotron superconducting synchrotron, a storage ring (booster), and a new linear accelerator [1]. The first of these three elements, a superconducting synchrotron with a magnetic rigidity of about 40 T m, was commissioned in March 1993 and has been in operation for physical experiments since then. In the difficult 1990s, the construction of a Nuclotron booster was dropped. During the operation of the Nuclotron, physicists repeatedly returned to the project of a booster whose main task would be to ensure high intensities of the accelerated beams. Options for the optical structures of the Nuclotron booster with circumferences of 50, 84, 100, 150, and 210 m were developed and analyzed, taking the options for its placement and assembly into account.

In 2009, work began at JINR on the design and construction of a new accelerator complex, NICA (Nuclotron-based Ion Collider fAcility) [2]. The concept was developed somewhat later [3], followed by the technical design of the NICA accelerator complex, whose purpose was to carry out an extensive program of fundamental research in relativistic nuclear physics, particle spin, radiobiology, and applied research [4–6].

The significance of the NICA complex for applied research is primarily determined by the possibility of obtaining beams of heavy charged particles with energies from several MeV per nucleon (MeV/n) to several GeV/n. Presently, there is no technology in Russia for using ion beams with an energy of 150–350 MeV/n to conduct research into and tests of promising products of semiconductor micro- and nanoelectronics, solid-state microwave electronics, and micromechanical systems that would allow predicting, evaluating, and controlling their radiation stability for further use in spacecraft and aviation systems. To solve this problem, a dedicated experimental station is being created at the NICA complex [7], with the start of research scheduled for 2023. In 2021, the creation of another experimental station [7] was started in order to increase the level of research in space radiobiology and simulate the impact of heavy charged particles of galactic cosmic radiation on biological objects, including cognitive functions of the human brain during long-term interplanetary flights.

In a more traditional JINR vein, experiments with relativistic heavy-ion beams on fixed targets are also being performed at the NICA facility [8, 9]. In 2018, studies were started at the new BM@N (Baryonic Matter at Nuclotron) experimental facility [8].

To ensure the high efficiency of such studies, the first stage of the NICA project in 2007–2012 consisted of upgrades to the Nuclotron and the existing injection complex [10, 11], which in 2018 allowed the first experiments to be conducted in relativistic nuclear physics and radiobiology with carbon, argon, and krypton beams [12]. At the next stage of the operation of the complex, experiments are planned on fixed targets using ion beams with a mass number greater than 100 and an intensity increased by three to four orders of magnitude. The implementation of this stage is based on the creation of a new injection chain of the main accelerator of the complex, the Nuclotron, including a linear heavy-ion accelerator (LHIA) and a booster synchrotron, called *the Booster*. In contrast to the counterparts that are closest in terms of both physical problems and the circumference of the ring — the SIS-18 synchrotron (German *Schwer Ionen Synchrotron* 18) [13] of the Heavy Ion Research Center (Gesellschaft für Schwerionenforschung, GSI) (Germany) and the AGS (Alternating Gradient Synchrotron) booster [14] of the Brookhaven National Laboratory (BNL) (USA) — the NICA Booster complex is designed to solve one more additional problem: to optimize the process of ion accumulation in the NICA *Collider*.

At the first stage of operation, the NICA Collider [3–6] must ensure collisions of beams of heavy-element nuclei such as $^{197}Au^{79+}$ or $^{209}Bi^{83+}$, with a center-of-mass energy of 4–11 GeV/n at average luminosity $L = 10^{27}$ cm^{-2} s^{-1}. This luminosity level is quite typical for high-energy hadron colliders, the Large Hadron Collider (LHC) (CERN, Switzerland) [15] and the RHIC (Relativistic Heavy Ion Collider) (BNL) [16], but the high luminosity to be achieved at the NICA Collider at low ion energies is limited by the maximum allowable frequency shift of the transverse betatron oscillations of particles caused by the self-field of the ion bunch. This shift is proportional to the circumference of the accelerator, and therefore the NICA Collider circumference, which is approximately 500 m, was chosen as the minimum that allows installing the detectors and technological equipment. This required developing a new procedure for the accumulation of beams in the collider rings with a small longitudinal acceptance of the accumulation system (due to the small circumference of the collider). The efficiency of the storage system depends on the momentum spread of the injected beam particles. The SIS-18 and AGS installations were built without beam cooling systems (SIS-18 was equipped with an electron cooling system (ECS) [17] eight years after its start of operation to expand the experimental capabilities of the accelerator), but the cooling system originally integrated into the NICA Booster design was to solve two problems: ensure the accumulation of ions at the injection energy (in the case of a low beam intensity from the source) and optimize the beam parameters at the collider input by cooling the beam at an intermediate energy. Accordingly, the optical structure of the booster was developed taking the conditions for the effective use of such a system into account. The ECS itself, developed and created at the Budker Institute for Nuclear Physics (BINP), Siberian Branch of the Russian Academy of Sciences, is the first system in Russia, besides the pioneering research [18], designed to ensure the operation of the accelerator complex for physical experiments.

A universal injection system that has been developed for ion sources of various types, with different pulse durations and beam intensities, allows implementing almost all previously used accumulation schemes in the phase space of transverse motion: from single-lap injection to multiply repeated multi-lap injection [19–21].

One of the main concerns in creating heavy-particle accelerators is to provide an ultrahigh vacuum in the beam chamber [22]. The typical residual gas pressure reached in previous-generation synchrotrons [13, 14] is 2–3 nPa. But the lifetime of ions is determined not only by pressure but also by the residual gas composition. In synchrotrons with a room-temperature magnetic system, a significant proportion of the residual gas concentration (10–20% of hydrogen concentration) is due to atoms of heavy elements: carbon, oxygen, etc. Superconducting magnets were chosen as the basis of the NICA Booster magnetic system. At cryogenic temperatures, the residual gases that include heavy atoms freeze out, and hydrogen can be efficiently pumped out by getter pumps.

The technology for the production of economical and reliable superconducting magnets developed at JINR in the course of building the Nuclotron was significantly advanced when constructing the NICA accelerator magnets [23], which allowed creating a modern technological process for their mass production [24].

When working with heavy ions, the booster ensures their acceleration to the energy required for recharging into 'bare' nuclei. This determined the magnetic rigidity of the accelerator at the level of 25 T m, corresponding to an $^{197}Au^{31+}$ ion energy of about 600 MeV/n, at which the ion stripping efficiency is close to 90%.

In addition, the power supply system for superconducting accelerator magnets was underlain by new technological solutions [25]. The use of a modern control system [26] allows creating highly efficient algorithms for setting up and switching over the operating modes using an extensive diagnostic system.

Thus, achieving the assigned goals required both a significant upgrade of the existing accelerator technologies and the development of new ones, never before used in Russia. All this makes the booster a new-generation synchrotron.

In this article, we describe the design and main systems of the booster, focusing on new technological solutions. In Section 8, we describe the methods for assembling and

testing Booster systems, and also present the results of the two first beam runs of the accelerator.

2. Booster design and systems

2.1 Booster tasks and parameters

The main tasks of the booster (Table 1) are as follows:

— accumulation of ions at an injection energy of 2.5×10^9 $^{197}Au^{31+}$ ions;

— effective acceleration of incompletely stripped ions, which is possible due to the ultrahigh vacuum in the beam chamber;

— formation of the required phase volume of the beam using an ECS at an energy of 65 MeV/n;

— acceleration of heavy ions to the energy required for their efficient stripping;

— fast (single-lap) extraction of the accelerated beam for its injection into the Nuclotron.

One of the booster's tasks is to accelerate an intense ion beam to an energy sufficient for an efficient recharging into 'bare' nuclei (see Section 4.1). At an $^{197}Au^{31+}$ ion extraction energy from the Booster equal to 578 MeV/n, the calculated value of the equilibrium charge is $Z = 78.7$, and the calculated stripping efficiency is close to 90%. The field growth rate of 1.2 T s^{-1} is optimal for all elements of the NICA injection chain. After the partial dismantling of the

Table 1. Parameters of beams and optical structure of the booster.

1. General data	
Ions	$2 \leqslant A/Z \leqslant 6.35$
Intensity of injected $^{197}Au^{31+}$ or $^{209}Bi^{35+}$ ions	2.5×10^9
Injection energy, MeV/n	3.2
Extraction energy, MeV/n	578
Injection revolution period, μs	8.5
Maximum magnetic hardness, T m	25
Circumference, m	210.96
Critical energy, GeV/n	3.25
Pressure, Pa	2×10^{-9}
Lifetime, s	5–10
Vacuum loss, %	< 5
HF harmonics during ion acceleration	5/1
95% beam emittance at single-lap injection, π mm mrad	15
2. Booster structure	
Number of superperiods	4
DFG type periods	24
Long straight section length, m	7
3. Structure dynamical characteristics	
Betatron oscillation frequencies: $Q_{x'}/Q_z$	4.8/4.85
Chromaticity: $\Delta Q_x/(\Delta p/p)/\Delta Q_z/(\Delta p/p)$	−5.1/ − 5.5
Orbit compaction factor	0.05
Acceptance: horizontal/vertical, π mm mrad	150/57

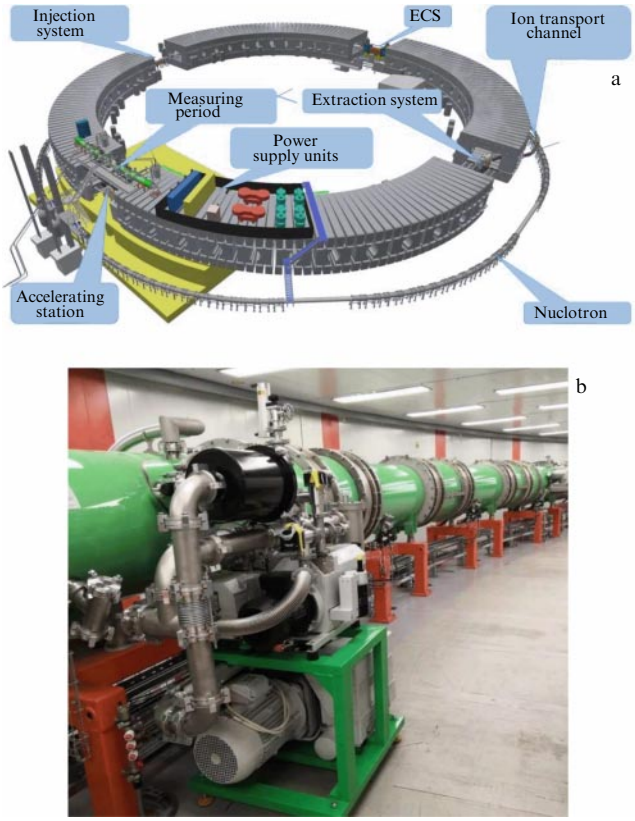

Figure 1. (a) Placement of the main booster systems (conventionally numbered along the beam path (counterclockwise) starting from the injection site). Straight gaps are designed to accommodate beam injection and extraction systems, accelerating HF stations, and the ECS. (b) Booster inside the iron yoke of the Synchrophasotron magnet.

Synchrophasotron magnet, a superconducting synchrotron with a circumference of about 210 m could be placed inside its yoke (Fig. 1a). The booster magnetic system consists of four quadrants, whose turning sections are located inside the Synchrophasotron magnet yoke (Fig. 1b), and the straight gaps coincide with the corresponding gaps of the Synchrophasotron magnet yoke.

The ion injection system in the booster includes several ion sources, a heavy-ion linear accelerator located in an annex to the Synchrophasotron building, and ion transport channels. The ions accelerated in the booster are completely stripped at its exit and transported to the Nuclotron through a special channel.

The optical structure of the booster consists of four superperiods, each of which includes five regular periods and one period that does not contain dipole magnets [4]. In designing the Booster, a regular period was initially envisaged based on an FGDG structure (F is a focusing lens, D a defocusing lens, and G a free gap) [7], the simplest from the standpoint of technological feasibility. One of the quadrupole lenses is then located in the middle of a long straight gap. This feature, on the one hand, allows optimizing the beam input and extraction systems, but, on the other hand, leads to serious problems in the design of the ECS and gives rise to dispersion in straight sections, which is undesirable for an accelerating system. After comparing several alternatives, the DFG structure was chosen, because the straight sections are free from lenses and there is no dispersion in them. A regular DFG period includes focusing (QF) and defocusing (QD)

quadrupole lenses, two dipole magnets (Ms), and four small free gaps designed to accommodate multipole correctors and the diagnostic equipment. A doublet of quadrupole lenses forms a single unit with a two-coordinate beam position controller. The parameters of the optical structure are given in Table 1. The operating point corresponds to the betatron numbers $Q_x = 4.80$ and $Q_y = 4.85$. The distance on the betatron resonance diagram from the operating point to the nearest coupling resonance, $Q_x - Q_y = 0$, and the distances to third-order resonances $3Q_x = 14$ and $Q_x - 2Q_y = 5$, are greater than the limit value $\Delta Q \geqslant 0.05$.

2.2 Straight section equipment

For a single single-lap injection, similar to that used at the Nuclotron, two devices are sufficient: an injection electrostatic septum (IES) with a sharp field boundary that delivers the injected beam to an equilibrium orbit without perturbing the circulating beam, and a kicker that compensates the inclination angle of the injected beam trajectory to the equilibrium orbit. The kicker is a pair of vertical inflector plates (IPs) installed parallel to the beam motion axis, with a voltage pulse applied to them (see Section 4.2).

To work with ion sources whose current pulse duration exceeds the particle revolution period in the booster, a more complex, multi-lap injection scheme must be used; if the beam coming from the source has a low intensity, it must be accumulated by means of multiply repeated injection pulses, including with the use of an ECS. To use such schemes, the closed orbit must be shifted in a controlled manner during injection. To do so, three pairs of inflector plates, IP1, IP2, and IP3, had to be placed in the first straight gap of the booster (Fig. 2) (see Section 4.3).

The high-frequency (HF) accelerating system manufactured at BINP [27] consists of two accelerating stations located one after the other in the second straight gap of the booster (Fig. 3), providing a total accelerating voltage up to 10 kV. When accelerating to full energy, the ion revolution frequency changes by about a factor of 10. To optimize the operating modes of accelerating stations, the acceleration multiplicity is changed at an intermediate energy. After injection, the beam is adiabatically bunched and accelerated at the fifth harmonic of the revolution frequency. The operating frequency of the accelerating stations for a given revolution frequency ranges from 587 kHz to 2.52 MHz. The maximum frequency for $^{197}Au^{31+}$ ions corresponds to a kinetic energy of 65 MeV/n. Upon reaching this energy and the maximum operating frequency, the beam is adiabatically unbunched on an intermediate magnetic field plateau and then bunched again at the first harmonic, 504 kHz. The change in the harmonic at the intermediate plateau of the magnetic field has been perfected in runs at the Nuclotron. The duration of this procedure is several ten milliseconds, but the possibility of maintaining the intermediate plateau for up to 1 s is envisaged in the design of the booster magnetic field in order to cool the beam whenever necessary by an ECS, which allows reducing the beam emittance and momentum spread.

In the case of fast (single-lap) extraction, the circulating beam is displaced into the region of the kicker linear field by a subsystem of controlled deformation (so-called controlled bump) of a closed orbit. The original design of the kicker [28] ensures a field amplitude up to 0.18 T, which is much higher than in other similar devices. At the exit from the kicker, a rechargeable target station is placed. The target material and thickness are optimized, depending on the type of accelerated

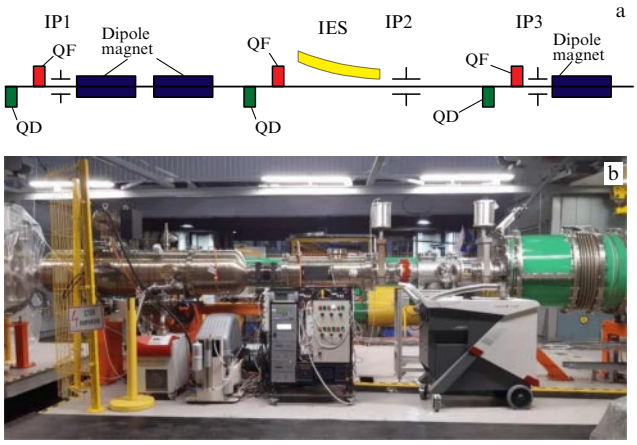

Figure 2. (a) First straight booster gap with injection system elements: large rectangles — dipole magnets, QF — focusing lenses, QD — defocusing lenses, IP — inflector plates, IES — injection electrostatic septum. (b) Photograph of the first straight gap of the booster with elements of the injection system.

Figure 3. Accelerating stations of the booster in the second straight gap. Elements of the measuring section are installed on the overpass, including a dipole magnet, a doublet of quadrupole lenses with inductive field sensors, high-current current leads, and an input of cryogenic liquids.

ions, and the design of the station allows replacing the target without violating the vacuum conditions in the booster beam chamber. After stripping, two sections of the septum magnet direct the beam into the ion transport channel to the Nuclotron [29]. The rechargeable target station, the elements of the extraction system located in the third straight gap of the booster (Fig. 4a), and the beam transport channel (Fig. 4b) were developed and manufactured at BINP.

Designed and manufactured at the BINP and located in the fourth straight gap, the booster ECS (Fig. 5 and Table 2) [30, 31] is intended to form the beam phase volume required for an efficient beam transfer to the Nuclotron and subsequent accumulation of ions in the collider [4, 32]. To obtain the minimum emittance of the beam extracted from the booster after stripping on a rechargeable foil, its transverse dimensions on the foil must also be minimized, which is achieved by beam cooling at an ion energy of 65 MeV/n. Achieving the required beam intensity in the collider requires about 80 beam injection cycles from the Nuclotron. The ions are accumulated in the longitudinal motion phase plane by a system of barrier stresses. The total longitudinal emittance of all the injected beams is about seven times higher than the acceptance of HF barriers. Efficient accumulation requires

Figure 4. (a) Elements of the fast extraction system in the third straight gap. (b) Booster–Nuclotron transport channel.

Figure 5. Fourth straight gap of the booster with the ECS.

the beams to be cooled both in the booster and in the collider. In addition, an ECS is planned to be used for the accumulation of ions in accordance with the multiple injection scheme (see Section 4.3). To reduce ion losses due to recombination with the cooling electrons, an operating mode with a hollow electron beam is provided.

After its delivery to JINR in 2017, the ECS was installed in its normal position, all the necessary subsystems were installed, and the field was adjusted in the solenoid of the cooling section, because field uniformity is crucial for the cooling system quality. The achieved value of the relative inhomogeneity of the field at the level of 2×10^{-5} corresponds to the best parameters worldwide. All ECSs have been tested with parameter values close to the design ones.

Table 2. Booster ECS parameters.

Electron energy, keV	1.5 – 60
Electron beam current, A	0.2 – 1.0
Cathode electron gun diameter, mm	30
Total length of the system, mm	6355
Length of the straight solenoid of the cooling section, mm	2522
Magnetic field in the cooling section, T	0.1 – 0.2
Field inhomogeneity in the cooling section, $\Delta B/B$	$< 10^{-4}$
Electron beam loss current, $\delta I/I$	$\leqslant 3 \times 10^{-5}$
Power consumption of the ECS at maximum magnetic field, kW	500

3. Magnetocryostat system

3.1 Development of technologies and improvement in parameters of superconducting magnets

Since the early 1970s, the development of the HEL accelerator complex has been associated with the use of superconducting magnetic technologies. Initially, the design concept of a new accelerator for heavy-element nuclei was developed on the basis of $\cos\theta$-type magnets with a field amplitude up to 4 T, and a prototype of such a magnet was studied. Subsequently, however, attention was mainly focused on the development of magnets whose field geometry is determined by an iron yoke, with a superconducting (SC) winding used to excite the field. The SC winding is made of a special tubular cable, which is a copper–nickel tube with a spiral winding of SC wires based on a niobium and titanium alloy NT-50. Two-phase (vapor–liquid) helium flows in the tube channel, cooling the winding to 4.5 K. The tubular superconducting cable developed for the Nuclotron magnets at the HEL was called the 'Nuclotron-type cable.' Due to the high current density in the SC winding, the dimensions and weight of such magnets are significantly lower than those of their analogues operating at room temperature.

Superconducting magnets with a Nuclotron-type tubular cable have the following main advantages over other types of SC magnets: (1) there is no need for a helium vessel of the cryostat; (2) the volume occupied by liquid helium in the magnet is significantly reduced; (3) effective cooling is ensured due to the absence of electrical (and hence thermal) insulation on the path of the heat flow from the superconductor to helium.

Bench tests have demonstrated the stable operation of magnets at a field variation rate of up to 8 T s^{-1}.

The advantages mentioned above have been clearly demonstrated in over a quarter of a century of Nuclotron operation. The straight dipole 'window frame' magnets used at the Nuclotron showed stable operation at fields up to 1.8 T, and that value was chosen as the design value for the booster magnets. To reduce capital costs of manufacturing and operating costs for employing cryostats, the Nuclotron magnet design was upgraded. In the early 2000s, a tubular cable design with a higher current density was developed (Fig. 6), which allowed increasing the peak current to 12 kA (instead of 6 kA at the Nuclotron) with almost the same outer

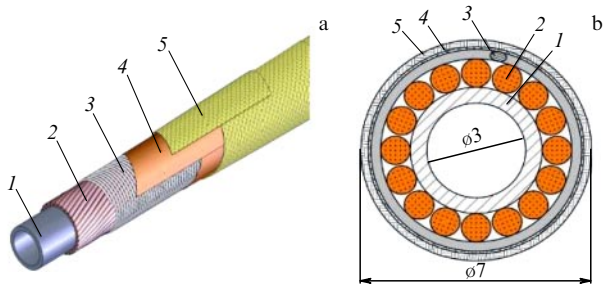

Figure 6. (a) Design of the tubular SC cable of the booster and collider magnets and (b) its cross section. *1* — cupronickel tube, *2* — SC wire, *3* — nichrome binding wire, *4* — polyimide insulation, *5* — glass tape impregnated with epoxy compound.

Table 3. Main characteristics of the NICA Booster dipole magnet.

Number of magnets in the ring	40 + 1 measuring magnets
Maximum magnetic rigidity $B\rho$, T m	25
Maximum magnetic field induction B_{max}, T	1.8
Minimum magnetic field induction over injection energy for ions with $A/Z = 6.25$ B_{min}, T	0.117
Effective magnet length L, m	2.2
Magnetic field variation rate dB/dt, T s^{-1}	1.2
Relative inhomogeneity of the magnetic field $\Delta B/B$ at a distance of 30 mm from the axial trajectory	$\pm 6 \times 10^{-4}$
Vacuum chamber aperture (horizontal/vertical), mm	128/65
Rotation angle, deg	9
Curvature radius, m	14.09
Gap between poles (horizontal/vertical), mm	150/67
Iron yoke length/width/height, m	2.14/0.31/0.228
Physical length of the magnet, m	2.36
Weight of the magnet, kg	850
Current at the maximum magnetic field, kA	9.68
Number of coils in the winding (per pole)	10(5)
Inductance, μH	630
Energy loss per cycle at $B = 1.5$ T, J per cycle	33.6
Total cycle time, s	4.02
Dynamical/static/total heat dissipation, W	8.4/4.4/12.8
Cable cooling channel diameter, mm	3.0
Cable length in the winding, m	54
Length of electric coupling cables of magnets, m	12
Pressure drop between supply and exhaust helium manifold, kPa	$\leqslant 27$
Maximum temperature of helium in the winding, K	4.65

diameter of the cable, which allowed magnets with a single-layer winding to be used in the booster (five coils per pole in dipole magnets) (Table 3), with a corresponding increase in the operational current to 10 kA. The required value of the magnetic rigidity of the booster corresponds to a turning radius of about 14 m (about 22 m in the Nuclotron magnets), which, with the same magnet length, leads to a noticeable increase in the sagitta, i.e., in the deflection of the trajectory in the magnet. To combine the requirements of operational economy and high horizontal acceptance, sector-type magnets with a yoke curvature radius of 14.09 m have been developed. To test such magnets, an original technology for measuring magnetic fields has been created. Particular attention was paid to reducing the static (in the absence of a magnetic field) heat gain and dynamical (at the design field cycle) heat release, which significantly affected the design of the iron yoke and the beam vacuum chamber. Power is supplied to the cryostat by new-generation high-current leads with high-temperature superconductors.

Full-scale prototypes of the booster dipole and quadrupole magnets were tested in 2013, and a modern production line for assembling, testing, and certifying magnets was put into operation in 2016 [24] (see Section 3.3).

3.2 Booster superconducting magnets

The magnetocryostat system [23] includes dipole magnets, quadrupole lenses, correctors, vacuum chambers, and a system for cooling them.

The booster dipole magnet is one with a superconducting winding made of a Nuclotron-type cable and with a curved laminated 'cold' yoke. The main characteristics of the dipole magnet are given in Table 3.

The booster dipole magnet is fixed in the cryostat with eight rods, such that, after it is cooled from room to liquid helium temperature, the spatial position of the optical axis of the magnet remains unchanged. The diameter of the vacuum casing of the cryostat is 640 mm. Between the vacuum casing and the magnet, a heat shield cooled by a stream of boiling nitrogen is installed. Feeding and draining helium collectors are attached to the bottom of the magnet. The single-layer bent winding of the magnet is made of a tubular superconducting cable developed at JINR for the Nuclotron magnets. A cooling channel inside the cable is for circulating the flow of two-phase (boiling) helium. The winding is placed in the gap of the iron yoke of the magnet, which feels the ponderomotive forces acting on the winding. The yoke, made of sheets of electrical steel 0.65 mm in thickness, welded together and attached to stainless steel angles and plates, is cooled by a helium flow coming from the winding.

Quadrupole magnets (Fig. 7) are installed in the vacuum casings in pairs. The main parameters of the NICA Booster quadrupole magnets are listed in Table 4.

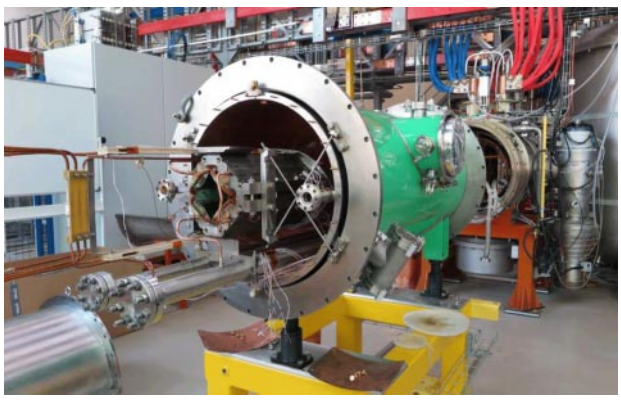

Figure 7. View of a quadrupole magnet with hyperbolic poles in the booster doublet cryostat.

Table 4. Main characteristics of the NICA Booster quadrupole magnet.

Number of magnets in the ring	48 + 2 measuring magnets
Maximum magnetic field gradient G_{max}, T m^{-1}	21.5
Minimum magnetic field gradient G_{min}, T m^{-1}	1.3
Effective magnet length l, m	0.47
Magnetic field gradient change rate dG/dt, T m^{-1} s^{-1}	14.3
Relative inhomogeneity of the magnetic field gradient $\Delta G/G$ at a radius of 30 mm	$\pm 6 \times 10^{-4}$
Distance from the axis to the pole, mm	47.5
Beam aperture vacuum chamber (horizontal/vertical), mm	128/65
Actual length of the magnet, m	0.66
Width and height of the yoke, m	0.226
Mass of the magnet, kg	110
Current at the maximum field gradient, kA	9.68
Number of coils in the winding (per pole)	8(2)
Inductance, μH	48
Energy loss per cycle at $G = 13$ T m^{-1}, J/cycle	3.33
Total cycle time, s	4.02
Dynamical/static/general/heat dissipation, W	0.84/3.0/3.8
Diameter of the cable cooling channel, mm	3.0
Length of the cable in the winding, m	19
Length of cables for the electrical coupling of the magnets, m	12
Pressure drop between the supply and the discharge helium collector, kPa	$\leqslant 25$
Maximum temperature of helium in the winding, K	4.65

3.3 Assembly and testing processes for superconducting magnets

In order to assemble and test superconducting magnets, a specialized process was created at the JINR Laboratory of High Energy Physics (LHEP) [24] (Fig. 8). The equipment for it, located in a specialized building with an area of 2600 m^2, provides

— production of superconducting cable;

— production of SC windings for various types of magnets;

— joining magnet cooling channels by welding and brazing;

— control over the geometric dimensions and vacuum tightness of the products;

— control over the electrical characteristics of the products;

— magnetic measurements at room and liquid helium temperatures;

— installation of the beam vacuum chamber in the magnet;

— assembling the magnet in the cryostat;

— cryogenic tests of magnets on six stands.

Cryogenic tests include training of the magnets, measuring static heat gain and dynamical heat release, measuring the hydraulic resistance of cooling channels and checking them for vacuum tightness, and measuring the qualitative characteristics of the magnetic field in the aperture.

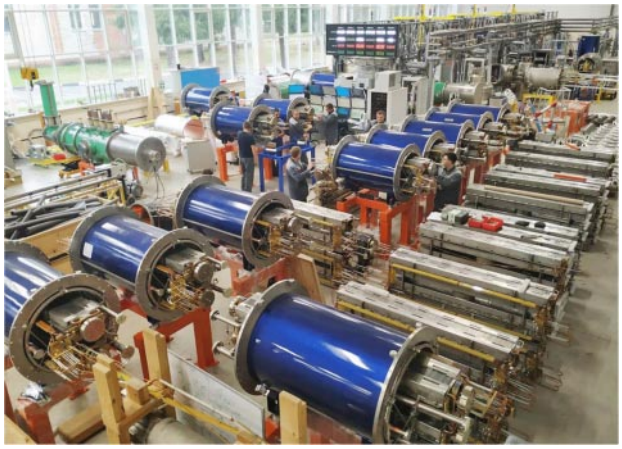

Figure 8. Superconducting magnet assembly and testing line.

With this specialized production line, 41 booster dipole magnets and 25 pairs of quadrupole lenses have been assembled and tested, and assembly and tests of all 80 collider double-aperture dipole magnets were completed. In total, 428 structural and 304 corrective SC magnets will be manufactured and tested for the booster, collider, and SIS-100 synchrotron of the FAIR (Facility for Antiproton and Ion Research) project (Darmstadt, Germany) [33].

4. Schemes of ion injection into the booster

4.1 Ion beam parameters during injection into the booster

The choice of the type of ion beam injection from the LHIA to the booster is determined by the most important parameters of the ion beam: its intensity, which strongly depends on the ratio of the atomic number to the ion charge of the ion beam, its emittance, and the injection energy. The A/Z ratio, on the one hand, is determined by the booster parameters: the energy of extracted ions that ensures a highly efficient stripping of ions transforming them into bare nuclei, and the radius of the booster dipole magnets (actually, its circumference). On the other hand, the A/Z ratio essentially determines the number of ions extracted from the source in one injection pulse.

The choice $A/Z \approx 6$ for $^{197}Au^{31+}$ or $^{209}Bi^{35+}$ heavy ions was the result of choosing, first, the energy of ion extraction from the booster as 578 MeV/n, at which the stripping efficiency is about 90%, and, second, the booster circumference equal to 210.96 m (the turning radius of the dipole magnets). Because the booster was placed inside the yoke of the LHEP Synchrophasotron magnets used for its radiation protection (Fig. 1b), the booster circumference was chosen equal to the Synchrophasotron circumference.

The decisive parameter for choosing the A/Z ratio is the intensity of the beam extracted from the ion source. The design value of the number of $^{197}Au^{31+}$ or $^{209}Bi^{35+}$ ions extracted from the Krion-N ion source is 2.5×10^9 per injection pulse [4]. Given the efficiency of beam transport in the Krion-N–LHIA–Booster–Nuclotron injection circuit, the number of ions extracted from the Nuclotron is 10^9 per injection pulse. To obtain the required luminosity of the collider, 6.6×10^{10} ions must be accumulated in it or 70 to 80 injection cycles must be executed, the exact number being

determined by the accumulation efficiency and the lifetime of ions in the collider during their accumulation. Thus, the choice of A/Z is determined by both the booster parameters and the ion source intensity, the latter being in turn determined by the maximum possible number of injections into the collider.

The choice of single-lap or multi-lap injection into the booster (see Section 4.3) depends on the ion source parameters, primarily on the pulse duration and emittance of the beam extracted from it. If the intensity of the beam coming from the ion source is insufficient, both single-lap and multi-lap injection can be implemented, the latter allowing the intensity of the ion beam accumulated in the booster to be increased severalfold.

The energy of ions injected into the booster, 3.2 MeV/n, along with the pressure of the residual gas in it, determine the lifetime of ions in the booster or the relative vacuum losses during injection, adiabatic capture, and acceleration. In order that the total relative vacuum loss of ions not exceed several percent, the circumference-averaged pressure in the booster should be at the level of 2×10^{-9} Pa (see Section 5).

4.2 Parameters and design of injection system elements

The booster injection system [4, 20, 34] (see Fig. 3) includes an injection electrostatic septum and a kicker, the latter consisting of three pairs of inflector plates, IP1, IP2, and IP3. The septum [4, 34] consists of two bent electrodes: a cathode, to which a high voltage is applied, and a grounded anode; the curvature of their surfaces corresponds to the input trajectory of the beam. With an IES length of 1.9 m and inter-electrode gap of 35 mm, the required maximum voltage at the cathode septum is 130 kV; the maximum field strength at the cathode edges does not then exceed 80 kV cm^{-1}. The thickness of the septum 'edge,' which is the anode, is 1 mm at its exit.

Inflector plates [4, 21, 34] are pairs of profiled plates installed vertically inside a separate vacuum box parallel to the beam motion axis. The plate power sources ensure independent unipolar charging and discharging of the plates that make up a pair. Modules of inflector plates IP1 and IP3 are placed in the booster cryostat, and the IP2 module, on the first straight gap, which is at room temperature. The parameters of the inflector plates are listed in Table 5.

The pulsed power supply system for the inflector plates [4, 34] includes five power sources that perform independent unipolar charging and discharging of the plates that make up the module (in the IP1 module, one of the plates is always grounded). The power sources are pulsed, with the design pulse repetition rate being 0.25 Hz in the case of a single beam injection into the booster. In the case of multiple injection, the pulse repetition rate is 10 Hz and the maximum number of consecutive pulses is three. The duration of the leading edge of the plate-charging pulse is 1 ms and the duration of the trailing edge of the plate discharge pulse is about 100 ns.

Table 5. Main parameters of IP1–IP3 inflector plates of the beam injection system in the booster.

Parameter	IP1, IP3	IP2
Effective length, mm	450	750
Maximum voltage on the plates, kV	65/20	50/15
Maximum electric field in the gap between the plates, kV cm^{-1}	6.4	10
Gap between plates, mm	102	93
Horizontal size of the healthy field area, mm	76	67
Vertical size of the healthy field area, mm	20	30
Quality of the field integral $(\Delta\int E\,\mathrm{d}l)/\int E\,\mathrm{d}l$, %	±1	±1

There are two modes of operation of the plate power system. In the single-stage mode, a potential is applied to only one plate of the module. In the two-stage mode, by the time the ions start being introduced, the potential is applied to both plates, one of which is then discharged, which leads to an abrupt change in the potential between the plates.

The plate charging–discharging scheme includes a charging DC voltage source, a thyristor pulse generator, a charging transformer, and a thyratron. The plate is charged by a pulse generator through a step-up transformer, with the thyristor key being the switch during charging. The plate is discharged by grounding it, with a thyratron used as a switch.

4.3 Methods for injecting ions into the booster

The booster accelerator equipment allows implementing several injection methods [19, 20, 35]: single single-lap, single multi-lap, multiple single-lap, and a multiple single-lap with the use of an ECS. The accumulation of ions is carried out in the horizontal phase plane of the booster.

Single-lap injection [19, 20] is the simplest method for beam injection into synchrotrons and storage rings. In the process of injection, the beam is introduced horizontally into the vacuum chamber of the booster and is placed on a specified trajectory of its circulation. The injected beam is placed by the inflector plate module IP3, which is switched off before the end of the first revolution of the injected particles in the accelerator. The primary scheme of a single single-lap injection is one with precise extraction ('placing') of the injected beam onto a closed orbit and full matching of its optical functions with the booster structure functions.

A single multi-lap injection [19, 20] consists in the gradual filling of the horizontal phase plane of the booster such that the injected ions are displaced along the phase plane due to coherent betatron oscillations so as to free space for newly injected ions at the exit of the booster injection system septum. Before the start of injection, a bump (distortion) of the closed orbit is created in the vicinity of the septum. The introduction of ions continues for two or three revolutions of the beam at the injection energy. If the fields in the inflector plates are constant, the closed booster orbit remains unchanged during the entire injection time, and ions are accumulated in the central region of the booster vacuum chamber.

To fill the horizontal phase plane with ions more compactly and reduce beam emittance after filamentation, the fields of the inflector plates are to be changed abruptly (in a two-stage pulse mode) with a transition to the second, plateau, stage at the beginning of the last revolution of the injected ions. In the first-level fields in the inflector plates, injection is done the same way as in the previously considered scheme with a constant closed orbit. At the second stage, the inflector plates are rearranged such that the center of mass of the accumulated beam at the output of PS3 is in a closed orbit in the booster.

Multiple single-lap injection without electron cooling [19, 20] consists in two- or three-fold repetition of single-lap beam injection (multiple injection stages). The design repetition rate of the injection stages is 10 Hz. At each stage, the previously

accumulated beam is brought to the septum edge, and the newly injected ions fill the region of the horizontal phase plane of the booster adjacent to the accumulated beam. The first stage amounts to implementing the scheme of a single single-lap injection with precise beam extraction into a closed orbit. At subsequent stages, before the introduction of ions, a local closed orbit bump is created in the injection system. The duration of the direct injection of ions does not exceed one revolution period of the beam, after which the inflector plates are turned off. With the described method (except for the first stage), as in the case of multi-lap injection, the horizontal phase plane of the booster is filled piecewise. The phase portrait of the beam after each injection stage depends on the mutual position of the closed orbit, the previously accumulated and newly injected beams, and the betatron functions of the injected beam. The position of the closed orbit and the accumulated beam is controlled by inflector plates, which allows both setting their voltage for each injection stage separately and changing it during the stage, and hence the transition to the second stage of the inflector plate pulses can be made immediately before the start of the injection. The position and the betatron functions of the injected beam are controlled by the electrostatic septum and the LHIA–Booster beam transport channel; these parameters can be changed only in the intervals between the injection stages. The use of different betatron functions and positions of the injected beam at different injection stages leads to a more compact phase portrait of the accumulated beam at the end of the injection.

As a result, several schemes of multiple single-lap beam injection can be implemented. These schemes can be classified according to two criteria: (1) the dependence of the betatron functions of the injected beam on the serial number of the injection stage, and (2) the use of a single-stage or two-stage pulse mode in the inflector plates of the injection system. In accordance with the first criterion, we divide the injection schemes into those with static and dynamical beam injection modes, and, according to the second criterion, into those with one-stage and two-stage operation of the inflector plates.

The use of electron cooling [30, 31] together with multiple single-lap injection allows increasing the intensity of the beam accumulated in the booster by a factor of 4 to 5 compared with the intensity of the injected beam for the lifetime of $^{197}Au^{31+}$ or $^{209}Bi^{35+}$ ions of about 5 s and the injection pulse frequency of 10 Hz [35], as well as decreasing the accumulated beam emittance during the cooling to a level determined by the number of accumulated ions and the Laslett shift of the betatron frequency $\Delta Q = 0.05$.

For the design operating point of the booster ($Q_x = 4.80$, $Q_y = 4.85$), the values of the 95% horizontal emittance of the accumulated beam after filamentation of the phase distribution of ions for the considered injection schemes are in the range from 15 to 135 π mm mrad, which does not exceed the booster acceptance of 150 π mm mrad.

We note that the transverse emittance at the output of the $^{209}Bi^{35+}$ ion source can be reduced by increasing the beam extraction pulse duration or by passing from single-lap injection to two- or three-lap injection. This feature of the ion source allows optimizing the emittance in the booster when using two- or three-lap injection.

The beam diagnostic system in the booster, which consists of 24 beam position monitors (pickups), two current transformers, and an ionization profilometer placed in the first straight gap, allows tuning the booster for the injection schemes described above. Two additional pickups are installed along the edges of the first straight gap for a more flexible adjustment of the closed-orbit bump. To study the collective effects that cause the development of transverse instabilities, standard split pickup electrodes are used. Schottky spectrum measurements (see Section 8.3) yield information about the excitation of longitudinal coherent oscillations of the ion beam that occur if longitudinal instabilities develop.

5. Vacuum system

5.1 Beam chamber vacuum system

During the acceleration of incompletely stripped ions, the main loss mechanism is a change in the charge state of the ion in its interaction with molecules and atoms of the residual gas. It is this effect that has until now limited the intensity of the accelerated Nuclotron beam. After the upgrade of the Nuclotron vacuum system, the orbit-average pressure of the residual gas is approximately 10^{-7} Pa, and significantly reducing it without changing the chamber design in the area of slow beam extraction is impossible.

Ensuring a residual gas pressure in the beam chamber of approximately two orders of magnitude lower than in the Nuclotron was one of the main tasks in the development of the booster [22]. The choice of the 3.2-MeV/n injection energy (at a minimum magnetic field of 0.117 T) was dictated by the maximum admissible loss of ions (below 5%) in collisions with atoms and molecules of the residual gas in the Booster vacuum chamber. The designed relative vacuum losses of $^{197}Au^{31+}$ or $^{209}Bi^{35+}$ ions in the booster will not exceed 2% for single injection with duration $\tau_{capt} \approx 50$ ms of adiabatic capture of ions at the injection energy and their further acceleration with the effective duration $\tau_{acc} = B_{min}/(2dB/dt) \approx 50$ ms, which is determined by the magnetic field $B_{min} = 0.117$ T during injection and the field growth rate $dB/dt = 1.2$ T s^{-1}. When calculating the effective duration of acceleration, the cross section σ_{capt} of ion interactions with the residual gas atoms and molecules depends on ion velocity v as $\sigma_{capt} \propto v^{-4}$. At the $^{197}Au^{31+}$ ion energy of 3.2 MeV/n, the cross section of their interaction with hydrogen molecules is estimated as $\sigma_{capt} \approx 5\times10^{-17}$ cm^2, and hence the estimated lifetime of such ions is about 5 s, which determines the pressure averaged over the booster circumference at the level of 2×10^{-9} Pa for the 3.2-MeV/n ion injection energy. We note that, for the triple injection scheme with a 200 ms duration, an adiabatic capture time of 50 ms, and an effective acceleration time of 50 ms, the relative vacuum loss of ions is 4% for the 5-s lifetime.

A specific feature of the superconducting booster with short straight warm gaps occupying 13% of its circumference is a small contribution to the loss of ions from their interaction with residual gases such as CO, CO_2, and CH_4, whose total molecular concentration in the warm sections is 10–20% of the concentration of hydrogen molecules. For synchrotrons with a magnetic system operating at room temperature [13, 14], this contribution either is comparable to, or even exceeds the contribution to the loss of ions due to interaction with hydrogen.

A feature of the booster vacuum conditions is the alternation of beam chambers at cryogenic and room temperatures. Moreover, the chambers inside fast-cycling superconducting magnets are heated, thereby leading to an

inhomogeneous temperature distribution of the beam chambers along the booster circumference.

The booster vacuum system includes 24 pumping stations located in arches, spaced 9 m apart, based on turbomolecular pumps, which will allow reducing the pressure to below 10^{-8} Pa. Cryogenic surfaces pump out all gases except hydrogen. To increase the pumping rate for hydrogen and achieve the required vacuum conditions at the level of 2×10^{-9} Pa, pumps based on nonsprayable getters are installed between all booster magnets. In straight gaps, magnetic discharge pumps are used in combination with sputtered titanium getters. Before the start of the accelerator run, in order to achieve the operating pressure and the optimal composition of the residual gas, the warm gaps are preheated to a temperature of 250 °C for 48 hours. One of the design features of the booster is the ultrahigh vacuum, 2×10^{-9} Pa [22].

5.2 Vacuum system of the insulating volume

As regards the insulating vacuum space of the cryostat, the booster magnetic system is divided into two half-rings. In each half-ring, a chain of 20 dipole magnets and 12 lens doublets is connected in parallel to the supply and discharge helium collectors. Hydraulic resistances of structural magnets and nonstructural elements are chosen such that the mass content of helium vapor at the output of each parallel cooling channel is about 90% in cyclic operation.

The vacuum casing of the booster is formed by joined cryostats of the magnets, joined by flange connections with a rubber seal. The casing is divided into the two booster half-rings, which have a separate insulating vacuum.

Twenty high-vacuum pumping stations, including diffusion pumps with a maximum capacity of 1750 l s^{-1}, are located along the circumference of the ring in the booster tunnel on the flanges of the vacuum casing of the accelerator and in the section of the booster measurement periods. The high-vacuum pumping stations are connected by an annular preevacuation collector, to which eight stations with rotary vane pumps and Roots-type pumps are connected via valves that are evenly spaced along the circumference of the ring and in the measuring period.

The vacuum system is tied by valves and gates with manual, electromechanical, and electropneumatic control. To protect the vacuum system from oil ingress during an emergency shutdown of the pumps, electropneumatic valves are installed on the preevacuation pump lines, which automatically close in the event of a power outage. Vacuum control in the insulating volume of the casing is carried out using TPG300 vacuum gauges and TPR018 and IKR060 sensors. Up to six leak detectors, which can be placed around the circumference of the ring whenever necessary, are designed to perform vacuum leak tests and analyze the gaseous medium in the insulating volume during the cooling of the ring.

6. Power supply system

6.1 System structure

Similarly to the Nuclotron, the power supply system for the magnetic elements of the booster (Fig. 9) is based on connecting all structural magnets in series [25, 36]. The main powerful source PIT11 generates the required current up to 10.0 kA with a specified growth rate up to 1.2 T s^{-1} for the field or up to 7 kA s^{-1} for the current in the common circuit.

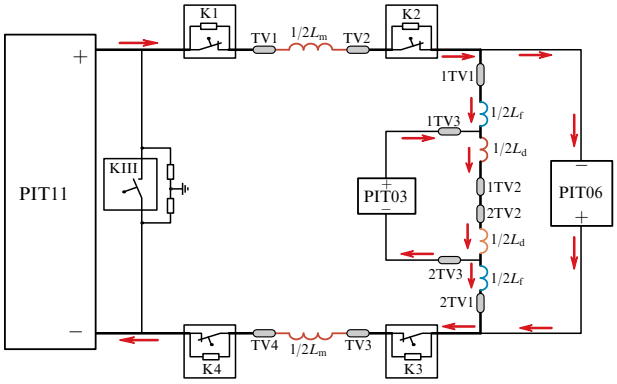

Figure 9. Schematic of the Booster power system. PIT11 — main source that feeds the series circuit of all structural magnetic elements; PIT03 and PIT06 — additional sources that correct the field in certain groups of elements, $L_m = 25.8$ mH — total inductance of dipole magnets, $L_f = L_d = 2.4$ mH — inductances of quadrupole focusing and defocusing magnets. TV1 to TV4 — high-current leads, 1TV1 to 1TV3 and 2TV1 to 2TV3 — current leads for connecting PIT03 and PIT06, K1 to K4 — thyristor keys, K — built-in key.

Two additional power supplies of significantly lower power, PIT06 and PIT03, are intended to adjust the position of the accelerator operating point. PIT06 allows changing the field gradient in both focusing and defocusing magnets simultaneously, and PIT03, only in defocusing ones. PIT06 and PIT03 can either add current to or take part of the current from the load.

To evacuate stored energy from superconducting elements in the event of superconductivity breakdown, thyristor switches K1 to K4 connected in series with a circuit of magnets (see Fig. 9) are used, controlled by a signal from an external detection system whenever normal-conductivity domains appear in the superconductor. When a signal occurs, the key opens and the energy accumulated in the magnets is dissipated in 0.5 s into the field damping resistors connected in parallel to the keys. The source is then locked, and its output is closed by built-in key K. The inductance of the groups of magnets and the value of the damping resistors are chosen such that the voltage relative to the 'ground' potential on the current leads during energy evacuation does not exceed 500 V. An example of the energy evacuation regime during the operating cycle of the source is shown in Fig. 10.

The power supply system is based on three precision current sources, PIT11, PIT06, and PIT03, unique in their parameters, developed and manufactured in cooperation between JINR and the Research and Production Enterprise (RPE) Limited Liability Company (LLC) RPE LM Invertor (Moscow).

Due to the unusual nature of the load (the superconducting magnetic system of the booster), the regime of cyclic energy transfer from a precharged storage device to the accelerator magnets and back is implemented in the PIT11 source. During operation, only the energy required to compensate for resistive losses in the connecting circuits of the system devices is taken from the supply grid. The accumulator is a battery of electrolytic capacitors with a total capacity of 60 F, charged to a voltage of 400 V. The energy of the accumulator is sufficient to ensure the design cycle of the magnetic field. The accumulator performs the important function of removing the cyclic load from the energy grid. The PIT11 maximum output current and

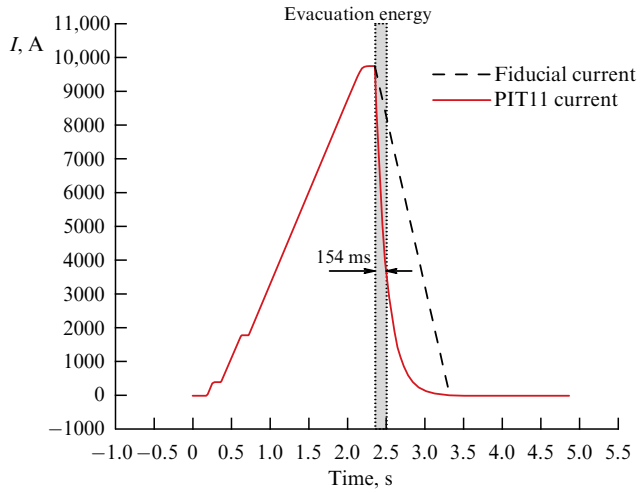

Figure 10. Schematic of the technological regime with current extraction and energy evacuation from magnets (154 ms time constant) on the current plateau with the design amplitude.

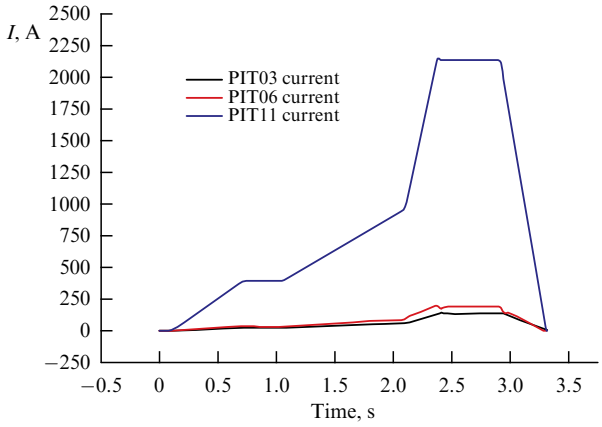

Figure 11. Normal operation cycle of three sources.

voltage are 11 kA and 260 V, the maximum peak of power consumption at the load is 2.86 MW, and the maximum power taken from the grid is not more than 300 kW; therefore, there are no losses in the high-voltage power cables of the laboratory power grid during the operation of the booster, and no effect on other consumers of electricity. In addition, the capacitor bank, being an ideal filter, completely eliminates grid harmonics in the rectified current, which could be a problem for high-power precision converter devices.

Structurally, PIT11 consists of 12 independent DC–DC converters connected in parallel, operating at a frequency of 5 kHz and phase-shifted relative to each other. As a result, the total source frequency is 60 kHz. This quality of the device provides ample opportunities to control the output voltage with high accuracy in order to obtain minimal pulsations while ensuring the necessary variation of the output current. The required relative levels of output current pulsations for the power system should not exceed 2×10^{-4} in dynamical sections and 2×10^{-5} in plateau sections.

The booster power supplies are several times more compact than the power supplies of the Nuclotron, which are classical thyristor rectifiers with an inductive capacitance filter. Due to the high conversion frequencies, there is no need to use massive filters and transformers. Digital modern control and regulation systems provide flexibility of settings and noise immunity in transmitting precise and fast signals. All power supplies are designed from the outset as part of a common system and are controlled from a single site via a high-speed fiber-optic interface for data exchange.

6.2 System for measuring currents

To control the currents of the booster magnets, a dedicated current measurement system (CMS) has been developed, which is an apparatus for collecting, processing, storing, and displaying information about currents in the booster power sources.

The CMS allows measuring currents in the range of 0.1–10,000 A with a relative accuracy reaching 1×10^{-4} dynamically and 2×10^{-5} statically, with a frequency of 800 Hz. The measuring part of the CMS consists of ultraprecise LEM ITZ FLEX ULTRASTAB current sensors, with a current measurement accuracy of 0.0065%. Specialized software has been developed for visualizing and archiving the information. The created CMS is the main tool for tuning the operating modes of the accelerator and monitoring its operation, but third-party equipment can also be used for control.

An example of the operation of three power sources of the magnetic elements for one operation cycle of the booster is shown in Fig. 11.

Overall, the decisions taken when creating the equipment for the power supply system of superconducting magnets of the booster made it possible to build a highly efficient precision converter power system.

7. Control system

The control system of the LHEP accelerator complex, which was created in the early 1990s simultaneously with the commissioning of the Nuclotron, actually consisted of various subsystems, integrating which into a common control system of the accelerator complex was practically impossible. From the beginning of the NICA complex's construction, a unified modern control system was needed, one capable of controlling a variety of heterogeneous units: ion sources, linear and cyclic accelerators, beam transfer devices and transport channels, etc. Among the several systems used at accelerator complexes, such as TANGO (TAco Next Generation Objects), Epics, and SCADA (Supervisory Control And Data Acquisition), the one chosen for the NICA accelerator complex was TANGO — a modern object-oriented system developed through the collaboration of several accelerator and software centers.

The TANGO Controls system is an open-source toolkit for controlling any hardware or software. Its development began at the research accelerator complex at ESRF (European Synchrotron Radiation Facility) (Grenoble, France) [37], and it is currently implemented in 49 research centers and institutes, including in Russia. TANGO is CORBA (Common Object Request Broker Architecture)-based middleware that allows linking disparate subsystem control elements and devices of the accelerator complex into a single distributed network control system. Software components compatible with the TANGO format have the ability to network with each other; all the jobs required to maintain network activity are hidden by TANGO, and the programmer deals only with a high-level interface that allows processing commands from devices, sending them to devices, and reading and recording data.

To implement a full-fledged control system, it was necessary to create lower-level programs (device servers) that control the equipment and collect data, data processing programs (high-level TANGO servers), and client applications that display data and provide the operator with hardware control capabilities. Different levels of client applications can be created: local, managing a specific subsystem, and more general, combining data received from various device servers. TANGO Controls is operating-system independent and supports C++, Java, and Python programming languages for all components.

The object-oriented approach implemented in TANGO was the decisive argument in favor of choosing this system for the NICA complex, which includes a large number of subsystems developed by different manufacturers and having their own control systems of various types. Such subsystems, for example, created based on Epics or SCADA, are integrated into the overall control system as device servers. In addition, possibilities open up for the widespread introduction, based on the same principle, of intelligent control systems with machine learning elements. Currently, work is underway to intellectualize the nitrogen supply system to the assembly and test line of superconducting magnets, and work has begun on the creation of an intelligent control system for the accelerating HF stations of the Nuclotron and the booster.

In 2012, the necessary infrastructure for the experimental segment of the NICA automatic control system (ACS) based on TANGO was created and was then successfully tested during a Nuclotron run [38]. Subsequently, all the Nuclotron systems were successively integrated into the new system, and relatively independent control systems for the assembly and test processes for superconducting magnets and the linear accelerator were created.

Several subsystems of the control system (CS) that are of the highest priority for launching the accelerator were created by the time of the first run of the booster. In general, the booster CS [26, 39] ensures the necessary infrastructure for reliable and safe execution of software and communication among various systems, and also provides some software services. The CS infrastructure includes a computer network on the scale of the accelerator facility, a computing cluster, and a distributed data storage system. Software services are designed to ensure the safe and reliable operation of the CS, its administration, collection, data storage, and access. These software services include systems for data archiving, authorization and access restriction, monitoring the CS software and hardware resources, and recording the CS status and operator actions. The client software provides operators with tools to control the accelerator systems and visualize the CS and beam diagnostics data. The CS contains several independent subsystems necessary for the operation of the accelerator, such as synchronization, thermometry, magnetic field cycle parameters, beam diagnostics, orbit correction, beam injection and extraction, HF control, vacuum control, and electron cooling.

Some of the booster subsystems, such as the HF power supply system, vacuum system, ECS, and interlock system, were manufactured by third parties. The interaction of the booster control system with third-party systems is achieved using top-level TANGO intermediate devices that implement the necessary interface for interaction and data exchange via various communication protocols.

Dividing the ACS components into several levels allowed moving most of the computing tasks and data processing and storage tasks from computers directly connected with equipment and sensors to a computer cluster that provides high performance, reliability, and easy scalability of computing power and disk space. The most effective way to organize the service layer is virtualization. Virtual servers have a number of significant advantages over physical ones:

— convenience of management: deployment, cloning, backup;

— division of tasks: a virtual server with the necessary guaranteed amount of resources is allocated for each CS task;

— more efficient use of computing resources (processor time, RAM, disk space) due to the fine tuning of resource allocation for each CS task;

— implementation of high-availability solutions: virtual servers can be automatically switched to other physical servers in case of problems with the host server.

For the booster ACS tasks, a cluster of several Supermicro physical servers is used, running the Proxmox virtualization system — a full-fledged open server platform for creating and managing a virtual infrastructure, including virtual machines, storage, virtual networks, and high availability clusters. The physical servers of the cluster are connected using a fast redundant 10-Gbit network. The most important component of the cluster is shared data storage: disk space available to all computers in the cluster to store the virtual machine disk images and CS data. The key parameters of the storage are high performance, reliability, and the ability to expand the available space without sacrificing performance. The booster CS uses one of the most promising modern solutions, CEPH storage, which is a free software object storage network that provides both file and block access interfaces [40].

A feature of the NICA CS is the broad use of web client applications that provide a convenient, elegant, and cross-platform interface for operators, developed on the basis of the original implementation of the specification for the TANGO device access standard via HTTPS (HyperText Transfer Protocol Secure) [41].

8. Assembling and testing booster systems. Results of the first runs

By the end of 2019, the manufacture of the main systems and elements of the booster was completed. According to the results of magnetic measurements, the dipole magnets were sorted in accordance with the condition of minimizing the perturbation of a closed orbit, and all elements of the magnetocryostat system were transported to the tunnel, installed in a regular position, and adjusted. On December 23, 2019, the procedure of stage-by-stage testing, assembly, and commissioning of the installation systems began. The assembly of the beam vacuum chamber was carried out sequentially joint by joint using a mobile clean zone. The elements of the injection and extraction systems were tested on special mounts before being installed into the ring. The accelerating stations were installed in the standard position and tested with a magnetic field cycle simulator. The main current source was tuned and the energy evacuation keys were tested on an equivalent load.

8.1 Ion injector

Simultaneously with the work described above, the heavy-ion injector was tuned, and the beam transport channel to the booster was assembled and tested. The main part of the injector is the LHIA linear accelerator, designed to accelerate

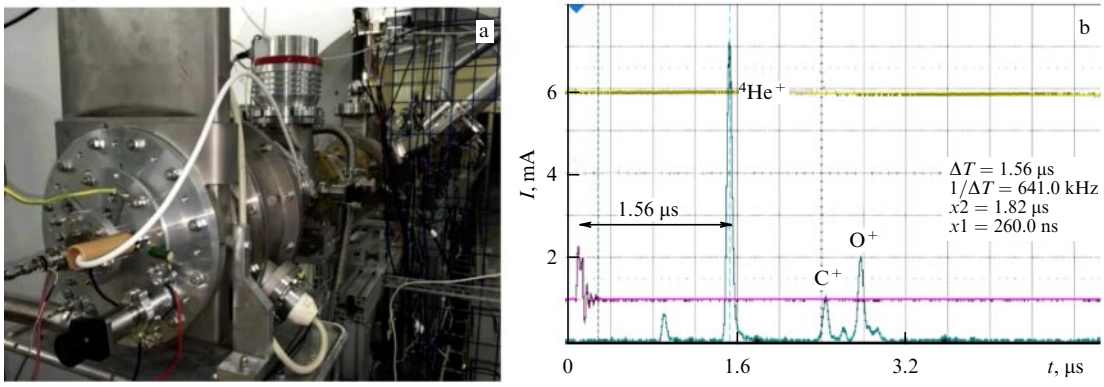

Figure 12. (a) Plasma source on the high-voltage platform of the LHIA preinjector and (b) time-of-flight mass spectrum of ions at the source output.

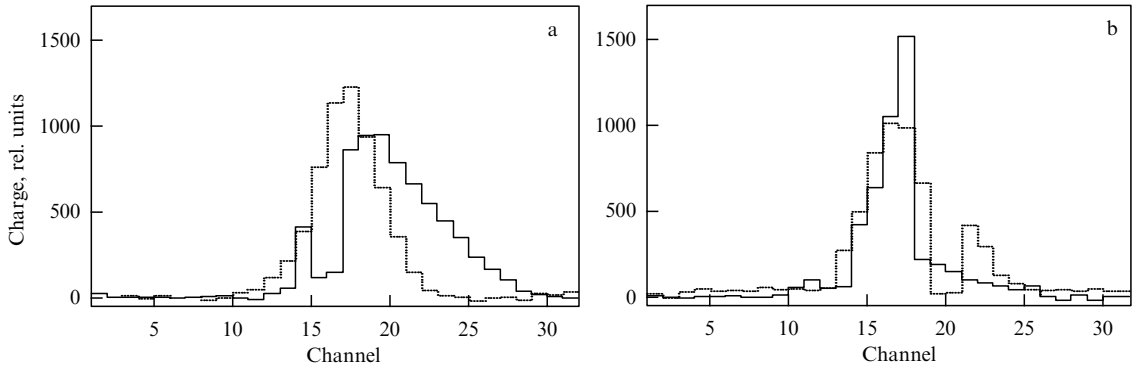

Figure 13. (a) Horizontal and (b) vertical beam profiles measured by multiwire profilometers (solid line — at the exit of the LHIA–booster transport channel, dotted line — in the middle of the channel); channel width 2 mm.

and inject ions into the booster with a mass-to-charge ratio $A/Z < 6.25$ and energy up to 3.2 MeV/n, with a peak current up to 10 mA in a pulse up to 30 μs in duration. The injector was developed and manufactured in cooperation with Bevatech (Germany) [42]. Three of its sections (one with a spatially homogeneous quadrupole focusing and two with drift tubes operating at a frequency of 100.625 MHz) were sequentially tested and tuned using a laser source in the period from 2016 to 2019 [43].

In preparing for the first booster run, attention was focused on choosing the particle type for acceleration. For measuring and adjusting the synchrotron orbit, the type of particle is of no fundamental importance, but for ease of interpreting the results, it is preferable to have a single-component beam, i.e., consisting of ions of only one kind in one charge state. In addition, to test a linear accelerator in a long-term operation mode, it is desirable that the ion mass-to-charge number ratio be sufficiently close to the maximum design value. As a result, $^4He^{1+}$ ions were selected, and a specialized plasma-type source was developed to produce them (Fig. 12) [44]. Of the entire spectrum of ions produced by it, only helium ions are stably accelerated in the LHIA.

The beam transport channel from the LHIA to the booster includes two dipole magnets, seven quadrupole lenses, six correctors, and a debuncher, which reduces the relative momentum spread from 5×10^{-3} to 10^{-3}. As a result of channel tuning, a beam transport efficiency of about 90% was achieved, and a current of up to 4 mA was obtained at the channel output, which is sufficient for reliable operation of all beam diagnostic devices in the booster. The supply currents of the quadrupole lenses obtained as a result of tuning coincided with good accuracy with predictions of the mathematical model of the channel: the maximum deviation from the calculated value of about 10% was obtained only for the first lens of the channel, and it was 1–3% for all other lenses. The distribution function of particles over coordinates (Fig. 13) is markedly non-Gaussian, but the half-width at the beam half-maximum does not exceed 14 mm at the channel output.

In the second run, the booster systems were also tuned using $^4He^{1+}$ ions, and then a transition was made to a laser source [45] optimized for generating a $^{56}Fe^{14+}$ ion beam.

8.2 Beam diagnostics

On December 4, 2020, upon the completion of the assembly and tests of the insulating vacuum volume and the cryogenic support system, the cooling of the ring began. From that moment, the Booster ACS was launched and a system to monitor the process involving the cryostat, including a thermometry system, was commissioned. On December 12, strictly on schedule, the magnetocryostat system was cooled to a temperature of 4.5 K and a test run for the booster systems started under conditions of superconductivity and beam injection and acceleration.

The program of the run and the composition of the booster equipment had been set during preparation in accordance with the tasks and time constraints. For particle injection, the simplest of the developed schemes, single single-lap, was used, in which only the IES and one pair of inflector plates are used (see Section 4.3). The devices of the beam extraction system were not used in the first run, although they were installed on the ring. The beam chamber evacuation

system consisted of the minimum number of vacuum posts necessary to cross the technological borderline of an ultrahigh vacuum, 10^{-8} Pa, and to initialize additional evacuation with ion and getter pumps.

After cooling the ring, the system for detecting transitions to the normal conductivity phase was adjusted and put into operation. Transition sensors, like those at the Nuclotron, are based on a bridge circuit, but due to the optimization of the structure of the measuring circuits, there was no need for individual balancing of sensors during their replacement and rearrangement. After balancing on the field plateau during adjustment, tuning the system sensors was not needed during the entire run.

At the next stage, the cycling system and the power supply system of the booster magnets were set up, and the energy evacuation system was tested. When working with a superconducting load, the power supplies provided a value of relative current instability on the magnetic field plateau at the level of 4×10^{-6}, which is better than the design value. However, in the increasing field sections, the best relative current instability attained was 4×10^{-4}. To improve this indicator, a suite of measures is planned to upgrade the main power source; the results of its implementation will be verified in forthcoming runs.

On December 19, 2020, work began on beam injection into the booster; as the work progressed, elements of the circulating beam diagnostic system were put into operation [44]. The beam intensity was measured by two current transformers, a fast one and a parametric one. The fast current transformer designed to measure the longitudinal beam profile with a resolution of approximately 0.2 ns was installed in the first straight gap directly at the output of the IES, such that it allowed measuring the intensity of both the beam coming from the transport channel and the circulating beam at the initial several hundred revolutions.

8.3 Results of first runs

The beam circulation regime was achieved without activating the magnetic field error-correction system at the level of the magnet supply current, the septum voltage, and the pulse amplitude on the inflector plates close to the calculated ones. The deviations in the beam orbit from the nominal, measured by beam position sensors, did not exceed ± 15 mm in the horizontal plane (and were slightly greater in the vertical plane), almost in exact agreement with the calculations. This is one of the most important results of the run, which is of fundamental importance for the NICA and FAIR projects, that the developed technology for the production, assembly, and testing of magnets ensures the design characteristics of the devices. An additional indicator of the manufacturing quality of the magnetocryostat system is its stable operation during a run with a magnetic field cycle for about 400 h.

To be able to measure the current and the beam position, injection with partial filling of the orbit was carried out [44]. The subsequent signal evolution is determined by two factors: the loss of particles during circulation and the spreading of the injected beam due to the spread in momenta, with gradual filling of the entire orbit. The particle loss in the first revolution does not exceed 10%. A more detailed analysis is practically impossible without the use of computer processing of the signals. When the HF system is switched on, the beam fragments into bunches in accordance with the multiplicity of the accelerating voltage.

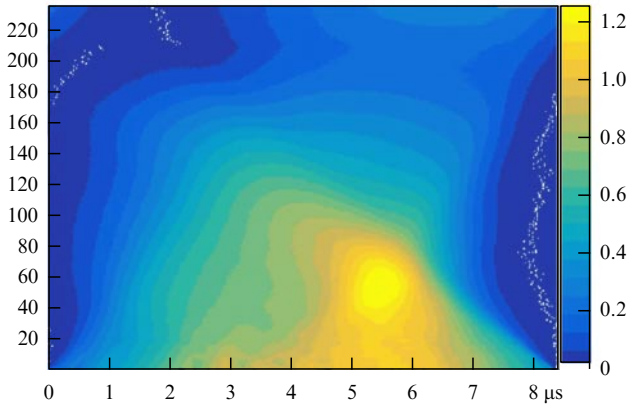

Figure 14. Computer processing of the fast current converter signal. Horizontal axis: time within one revolution, vertical axis: revolution number. Color encodes the density of particles in relative units.

To adjust the adiabatic bunching and beam acceleration regimes, it is planned to use the methods of computer tomography of bunches [46], which allows studying the evolution of the particle distribution function on the phase plane of longitudinal motion. These methods have been tested at the Nuclotron [47]. In the framework of the Booster ACS, the bunch computer tomography algorithm is implemented as a TANGO device that uses a mathematical model of longitudinal motion dynamics to process signals from the fast current transformer and the accelerating HF system and to visualize the results. In the first booster run, the algorithm was used in a test mode, in which rotational measurements were made of the longitudinal profile of the bunch (Fig. 14) circulating in the booster on the magnetic field plateau.

The closed orbit and linear optics of the booster are corrected based on a mathematical model of the accelerator, built in accordance with the results of magnetic measurements for all elements of magnetic optics and the measured values of the imbalance currents of the focusing and defocusing lenses and the supply currents of the correcting magnets. In addition, the mathematical model must include the actual mounting errors of each magnetic element, which are revealed during the accelerator tuning. To determine the closed orbit of ions, a system was created based on 24 two-coordinate beam position sensors (pickups), whose signals are preliminarily amplified and then digitized and processed by specialized Libera Hadron processor units. The data from the beam position monitors are used both for lap-by-lap analysis algorithms and for measuring the position of a closed orbit.

The lap-by-lap analysis is carried out in the presence of coherent beam oscillations excited by a measuring kicker or due to beam injection with a displacement from a closed orbit [44]. This analysis allows restoring the parameters of the mathematical model in a small section of the accelerator. In the first run, such an algorithm, implemented in the form of a TANGO device, was used to plot the phase trajectories of the beam center of gravity in two principal planes at the injection point using signals from the two pickups closest to it, and to calculate the structure functions, the closed orbit position, and the fractional part of the betatron number (Fig. 15). The Twiss parameters obtained in the measurements were $\alpha_{x,\,y} = 0.536/(-0.59)$, $\beta_{x,\,y} = 6.071/6.044$, and $\gamma_{x,\,y} = 0.212/0.223$; the Courant–Snyder (emittance) invariants for the center of mass of the injected bunch are $J_{x,\,y} = (4.558/0.259)\,\pi$ mm

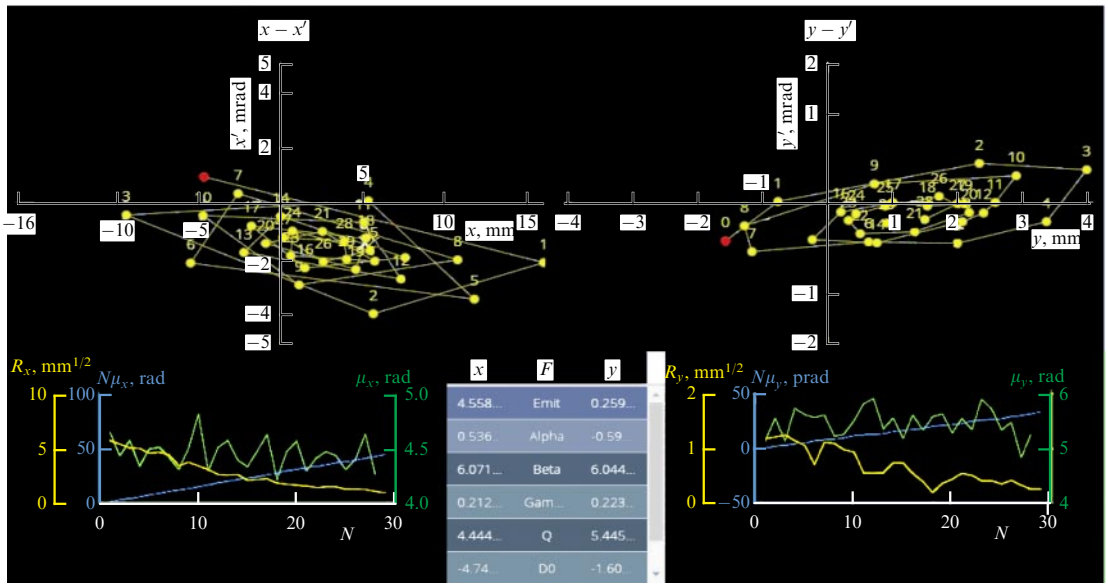

Figure 15. Image from the monitor of beam position sensors. Red dot corresponds to the beam parameters on the coordinate–angle phase plane after injection, yellow dots with a number k correspond to the beam parameters on the coordinate–angle phase plane after its kth rotation. Results of signal processing of two pickups in the vicinity of the injection point: signals from pickups as functions of the lap number (lower curves), phase trajectories of the beam center of gravity in two main planes (upper graphs, left and right in the horizontal and vertical plane), structure function values, and the fractional part of betatron numbers (table in the center). R_x and R_y are the normalized amplitudes of horizontal and vertical betatron oscillations of ions, $N\mu_x$ and $N\mu_y$ are phase increments of the horizontal and vertical betatron oscillations per N ion revolutions, μ_x and μ_y are the phase increments of horizontal and vertical betatron oscillations for each revolution.

mrad; the transverse coordinates of the point of entry of ions into the injection section for the center of mass of the bunch are $D0_{x,\,y} = -4.74/(-1.6)$ mm, and the betatron numbers are $Q_{x,\,y} = 4.444/5.445$ (see the table in the center of Fig. 15).

To correct the closed orbit and restore the mathematical model of the entire ring, it is planned to use the method of harmonic analysis and measure the response matrix of the closed orbit to the effects of corrective magnets. The first run was focused on testing the pickup and correction system. Preliminary tuning of the closed orbit of the beam transport channel from the LHIA and injection devices allowed achieving a beam intensity at the level of 7×10^{10} circulating $^4He^{1+}$ ions, which is equivalent in terms of current to the design intensity of 2×10^9 $^{197}Au^{31+}$ ions.

We note that, as the design value of the circulating ion current was achieved, no beam instabilities, coherent oscillations, or other collective effects were observed. To study coherent oscillations, the booster provides a special diagnostic system that includes standard split beam position sensors and a Schottky pickup (see Section 4.3). But because the design current of circulating ions is less than the threshold currents for the development of instabilities, the booster does not contain a feedback system, which is a feature distinguishing it, for example, from the synchrotron of the FAIR SIS-18 accelerator complex [48], in which collective effects play a significant role.

The typical lifetime of ions is approximately 1.32 s [49]. The main mechanism leading to losses is the change in the charge state of ions upon interaction with molecules and atoms of the residual gas. Given the cross sections of charge exchange processes, the measured lifetime value corresponds to the orbit-averaged density of the residual gas in the beam chambers, deduced from the measured spectrum of this gas and the circumference-averaged pressure value of 2×10^{-8} Pa [49], which is in good agreement with the readings of the vacuum gauges. Calculated from these data, with the lengths of all 'warm' and all 'cold' sections taken into account, the average pressure along the booster ring was about 0.14 nTorr (19 nPa).

After optimizing the tuning of the beam circulation at the injection energy, the HF accelerating system was tuned, the regimes of adiabatic capture and acceleration during injection into an increasing field were tested, and experiments were carried out to accelerate ions to an energy of 100 MeV/n. The choice of the maximum ion energy during the first run of the booster was determined by the radiation conditions of its operation without the extraction system. The beam was first accelerated and then decelerated, after which it was damped onto the vacuum chamber walls.

At the end of the run, a comprehensive testing of the power supply system of the magnets and the cryogenic and magnetocryostat systems was done in a magnetic field cycle operation with maximum stably attained parameters. Achieving the design values of the magnetic field and its growth rate required breaking in the magnetic elements and their connections to transitions to the normal phase. When operating with small currents of the main source, not a single transition was recorded. When increasing the current to the design level of 10 kA, more than 100 transitions were recorded. Although all magnets had been broken in on the test bench, some of them showed up to 17 transitions (Fig. 16).

As a result, a cycle was set up with two plateaus corresponding to the injection energy and the electron cooling energy in the area of the increasing field; on the third, upper, plateau, a field of 1.8 T was attained, and a field rate of change of 1.2 T s^{-1} was ensured in the increasing and decreasing field areas, which fully corresponds to the design parameters of the cycle (Fig. 17).

By the start of the second run (September 2021) [50], the installation of the beam transfer channel from the booster to

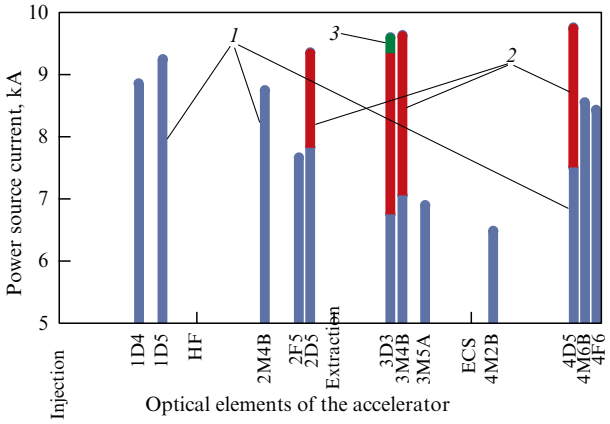

Figure 16. Current amplitude in superconducting magnetic elements during transition and number of detected transitions in them (*1* — one transition, *2* — two transitions, *3* — three transitions). D — defocusing lens, F — focusing lens, M — magnet. Number in front of the letter is the number of the superperiod, number after the letter is the number of the period in the superperiod. For magnets M, letters A and B denote the first and second magnet.

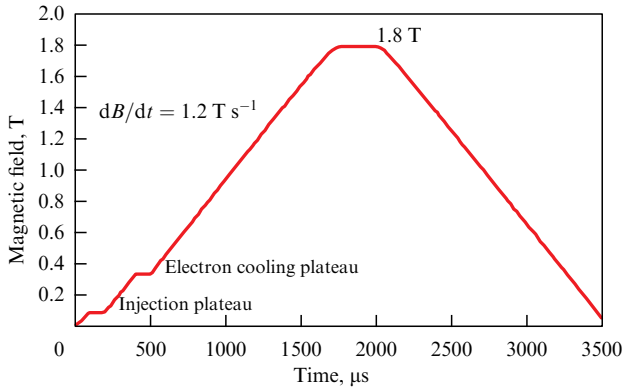

Figure 17. Timeline of the magnetic field cycle with two plateaus in the increasing field area at the third, upper, plateau. Magnetic field is 1.8 T.

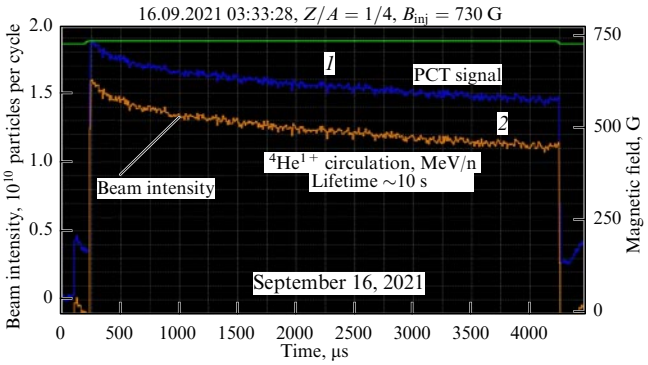

Figure 18. Snapshot of the monitor of a parametric current transformer. Results of measuring the intensity of the circulating $^{4}He^{1+}$ ion beam with an energy of 3.2 MeV/n using a parametric current transformer (PCT): curve *1* — PCT signal, curve *2* — number of circulating particles.

the Nuclotron was completed. Testing all of its systems was the main goal of the run. The pressure of the residual gas in the beam chamber was significantly reduced compared to that in the first run. The lifetime of $^{4}He^{1+}$ ions on the injection plateau was more than 10 s (Fig. 18), and the $^{56}Fe^{14+}$

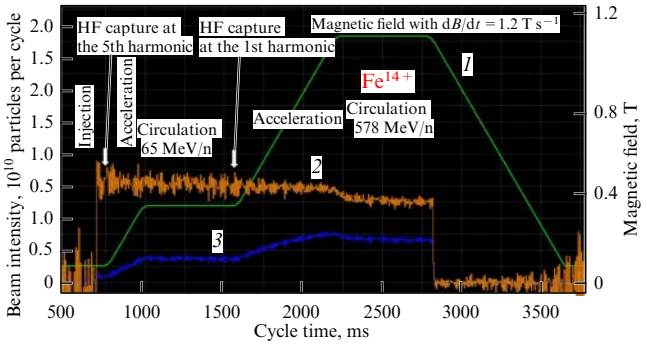

Figure 19. Results of measuring the intensity of the circulating $^{56}Fe^{14+}$ ion beam using PCT during injection, bunching, and acceleration. Curve *1* — magnetic field, curve *2* — number of circulating particles, curve *3* — PCT signal.

lifetime, more than 5 s, which corresponded to a pressure of approximately 5×10^{-9} Pa. With the $^{56}Fe^{14+}$ ion beam, adiabatic capture into the acceleration mode at the fifth harmonic of the accelerating field was carried out with an efficiency of more than 95% (Fig. 19). The beam was accelerated almost without loss to an energy of 65 MeV/n, unbunched at that energy and bunched again already at the first harmonic, and then accelerated to the design energy of 578 MeV/n at the magnetic field increase rate of $dB/dt = 1.2$ T s^{-1}. The loss of $^{56}Fe^{14+}$ ions at the injection energy due to interaction with the residual gas was 1–2% at a beam intensity up to 2.5×10^{8} ions. During the acceleration of ions to their maximum energy, practically no transverse ion losses were observed (see Fig. 19). Ions were extracted from the booster and transported through the booster–Nuclotron channel with a total beam extraction and transport efficiency of about 70%.

During the second booster run, $^{56}Fe^{14+}$ ions were cooled at the injection energy of 3.2 MeV/n [50]. The orbit of the circulating beam was corrected with the field in the cooling section solenoid increased to 700 G. With the solenoid switched on, the beam was accelerated, and no additional losses were observed. The electron beam recuperation mode with a current up to 160 mA was provided. The cooling process was diagnosed by recording the Schottky shot noise of the beam, measured with one of the standard beam position sensors, and using an ionization profilometer based on microchannel plates. As a result of fine tuning of the electron energy and optimization of the mutual position of the electron and ion beams at the injection energy, ion cooling was achieved. The root-mean-square relative spread of ions in momentum, measured from the Schottky noise spectrum, was approximately 5×10^{-4} during injection. As a result of the cooling, it was reduced to approximately 1.7×10^{-4} (Fig. 20). With an electron beam current of 46 mA, the characteristic cooling time of the longitudinal degree of freedom was about 0.2 s. Transverse cooling was detected by an ionization profilometer, while the squared width of the horizontal and vertical beam profiles (emittance) decreased with a characteristic time of about 2 s.

9. Conclusion

As a result of two runs with $^{4}He^{1+}$ and $^{56}Fe^{14+}$ ion beams carried out on a new superconducting synchrotron of the NICA–booster complex in November–December 2020 and

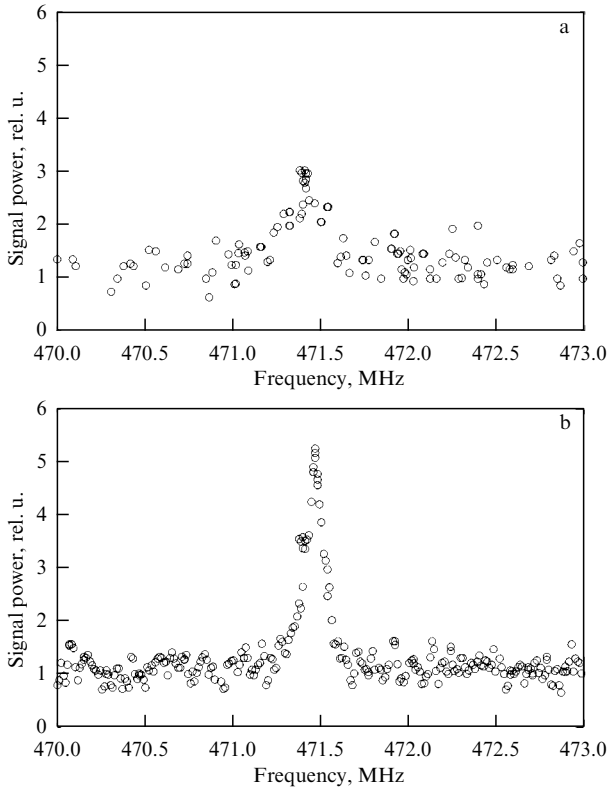

Figure 20. The measured Schottky spectrum at the fourth harmonic of the ion revolution frequency: (a) before cooling and (b) after cooling.

September 2021, all of its working systems were tested and tuned, and the main design parameters of the accelerator were achieved. After the installation at the Nuclotron of the devices for beam injection from the booster, which is scheduled for the nearest future, the entire chain of heavy-ion accelerators, LHIA, booster, and Nuclotron, will be ready to resume the research program. The first experiments with heavy-ion beams are scheduled for 2022. In the course of the work, a specialized 'Krion-6T' source [51] will be used, designed to generate beams of heavy ions up to gold ($^{197}Au^{31+}$) and bismuth ($^{209}Bi^{35+}$).

The authors are grateful to colleagues from the Alikhanov Institute of Theoretical and Experimental Physics, from the BINP, Siberian Branch of the Russian Academy of Sciences, from LLC RPE LM Invertor, and all the staff of LHEP Accelerator Department 1, JINR, who took an active part in the development, manufacture, and launch of the booster systems.

Added in proofs. While waiting for this article to be published, in January–March 2022, joint work of the LHIA, booster, and Nuclotron with carbon ion beams was carried out [52]. The carbon ion beams extracted from the Nuclotron were used for experiments at the BM@N facility to study short fluctuations of paired nucleons of carbon nuclei with high and opposite momenta at a low center-of-mass momentum. Xenon ion beams formed with a specialized 'Krion-6T' ion source [51] were accelerated in the LHIA, booster, and Nuclotron in October–November 2022. In December 2022–January 2023, experiments are planned with these beams to study baryonic matter at the BM@N facility. The installation of equipment for the collider rings, which began in December 2021, continued during 2022. Simultaneously, work continues at the JINR on the construction of a building to accommodate the main experimental facility of the NICA complex, the collider with its transportation channels. Production of the main systems and devices of the collider is at the final stage.

References

1. Baldin A M et al. "Uskoritel'nyi kompleks tyazhelykh ionov" ("Heavy ion accelerator complex"), Preprint JINR 9-11796 (Dubna: JINR, 1978)
2. Trubnikov G et al., in *Particle Accelerator. Proc. of the 11th European Conf., EPAC 2008, Genoa, Italy, June 23–27, 2008* (Eds I Andrian, C Petit-Jean-Genaz) (Geneva: CERN, 2008) p. 2581
3. Kekelidze V et al. *Phys. Part. Nucl. Lett.* **9** 313 (2012); *Pis'ma Fiz. Elem. Chast. At. Yad.* **9** 521 (2012)
4. Averichev A S et al., in *Tekhnicheskii Proekt Uskoritel'nogo Kompleksa NICA* (Technical Design Project of the NICA Accelerator Complex) Vol. 1 (Eds I N Meshkov, G V Trubnikov) (Dubna: JINR, 2015) p. 17
5. Kekelidze V D et al. *Eur. Phys. J. A* **52** 211 (2016)
6. Agapov N N et al. *Phys. Usp.* **59** 383 (2016); *Usp. Fiz. Nauk* **186** 405 (2016)
7. Slivin A et al., in *Proc. of the 12th Intern. Particle Accelerator Conf. IPAC, 24–28 May 2021, Campinas, Brazil* (Eds L Lin et al.) (Geneva: JACoW Publ., 2021) p. 946, https://doi.org/10.18429/JACoW-IPAC2021-MOPAB300
8. Kapishin M N "Eksperiment s fiksirovannoi mishen'yu dlya izucheniya barionnoi materii na nuklotrone (BM@N)" ("Fixed target experiment for studies of baryonic matter at the nuclotron (BM@N)") *Yad. Fiz. Inzhiniring* **7** 543 (2016)
9. Henning W F, in *Proc. of the Europhysics Conf. EPAC, 5–9 July 2004, Lucerne, Switzerland* (Ed. P-J-G Christine) (Geneva: JACoW Publ., 2004) p. 50
10. Trubnikov G V "Sinchrotron relyativistskikh tyazhelykh ionov Nuklotron v uskoritel'nom komplekse NICA" ("Synchrotron of relativistic heavy ions Nuclotron at the NICA accelerator complex"), Doctoral Dissertation (Phys.-Math. Sci.) (Dubna: JINR, 2012)
11. Butenko A V "Uskorenie puchkov tyazhelykh ionov s massovym chislom bolee 100 v sverkhprovodyashchem sinkhrotrone Nuklotron" ("Acceleration of beams of heavy ions with a mass number lager than 100 in the superconducting synchrotron Nuclotron"), PhD Thesis (Tech. Sci.) (Dubna: JINR, 2012)
12. Sidorin A et al., in *Proc. of the 26th Russian Particle Accelerator Conf., RUPAC'18, Protvino, Russia, 1–5 October 2018* (Eds M V Kuzin, V R W Schaa) (Geneva: JACoW Publ., 2018) p. 49, https://doi.org/10.18429/JACoW-RUPAC2018-TUZMH04
13. Blasche K, Böhne D, in *Proc. of the 13th IEEE Particle Accelerator Conf., PAC'1989, 20–23 March 1989, Chicago, IL, USA* (Eds F Bennett, K Joyce) (New York: IEEE, 1989) p. 27
14. Weng W T et al., in *Proc. of the 14th IEEE Particle Accelerator Conf., PAC'1991, 6–9 May 1991, San Francisco, CA, USA* (New York: IEEE, 1991) p. 52
15. Lefèvre P, Pettersson T (Eds), The LHC Study group "The Large Hadron Collider: Conceptual Design", CERN/AC/95-05 (LHC) (Geneva: CERN, 1995)
16. Ozaki S "RHIC commissioning and first results", in *Proc. of the 19th IEEE Particle Accelerator Conf., PAC'2001, 18–22 June 2001, Chicago, IL, USA* (New York: IEEE, 2001)
17. Steck M et al. "Commissioning of the electron cooling device in the heavy ion synchrotron", in *Proc. of the 6th European Particle Accelerator Conf., EPAC'1998, 22–26 June 1998, Stockholm, Shweden* (Eds S Myers et al.) (Stockholm, 1998) p. 1347
18. Budker G I et al. *Sov. Atom. Energy* **40** 50 (1976); *Atom. Energ.* **40** 49 (1976)
19. Bracco C, in *Proceedings of the CASCERN Accelerator School: Beam Injection, Extraction and Transfer, Erice, Italy, 10–19 March 2017* (CERN Yellow Reports: School Proc., Vol. 5/2018, CERN-2018-008-SP, Ed. B Holzer) (Geneva: CERN, 2018) p. 131
20. Volkov V I et al. *Phys. Part. Nucl. Lett.* **11** 675 (2014); *Pis'ma Fiz. Elem. Chast. At. Yad.* **11** 1045 (2014)

21. Bulanov V A et al. *Phys. Part. Nucl. Lett.* **13** 978 (2016); *Pis'ma Fiz. Elem. Chast. At. Yad.* **13** 1527 (2016)
22. Bazanov A M et al. *Phys. Part. Nucl. Lett.* **13** 937 (2016); *Pis'ma Fiz. Elem. Chast. At. Yad.* **13** 937 (2016)
23. Khodzhibagiyan H et al., in *Proc. of the XXIII Russian Particle Accelerator Conf., RuPAC'2012, September, 24–28, 2012, St. Petersburg, Russia* (Geneva: JACoW Publ., 2012) p. 149
24. Kostromin S A et al., in *Proc. of Intern. Particle Accelerator Conf. IPAC'2016, Busan, Korea, May 8–13, 2016* (Eds C Petit-Jean-Genaz et al.) (Geneva: JACoW Publ., 2016) p. 1215, http://doi.org/10.18429/JACoW-IPAC2016-TUPMB051
25. Karpinskii V N "Sistemy pitaniya i evakuatsii energii v bystrotsikliruyushchikh sverkhprovodyashchikh sinchrotronakh" ("Power supply and energy evacuation systems in fast cycling superconducting synchrotrons"), PhD Thesis, Abstract (Tech. Sci.) (Dubna: JINR, 2012)
26. Andreev V et al. *Phys. Part. Nucl. Lett.* **17** 574 (2020); *Pis'ma Fiz. Elem. Chast. At. Yad.* **17** 615 (2020)
27. Kurkin G Ya et al., in *Proc. of the XXIV Russian Particle Accelerator Conf., RuPAC'2014, Obninsk, Russia, 6–10 October 2014* (Geneva: JACoW Publ., 2014) p. 26
28. Alexandrov V, Tuzikov A, Fateev A, in *Proc. of the 25th Russian Particle Accelerator Conf., RuPAC'2016, St. Petersburg, Russia, November 21–25, 2016* (Geneva: JACoW Publ., 2016) p. 566, https://doi.org/10.18429/JACoW-RuPAC2016-TUCAMH02
29. Tuzikov A et al., in *Proc. of the 26th Russian Particle Accelerator Conf., RUPAC'18, Protvino, Russia, 1–5 October 2018* (Eds M V Kuzin, V R W Schaa) (Geneva: JACoW Publ., 2018) p. 52
30. Bubley A V et al. *Proc. of the Workshop on Beam Cooling and Related Topics, COOL'17, Bonn, Germany, 18–22 September 2017* (Geneva: JACoW Publ., 2017) p. 22, https://doi.org/10.18429/JACoW-COOL2017-TUM11
31. Smirnov A V et al., in *Proc. of the 26th Russian Particle Accelerator Conf., RUPAC'18, Protvino, Russia, 1–5 October 2018* (Eds M V Kuzin, V R W Schaa) (Geneva: JACoW Publ., 2018) p. 188
32. Kostromin S A et al. *Phys. Part. Nucl. Lett.* **9** 322 (2012); *Pis'ma Fiz. Elem. Chast. At. Yad.* (4–5) 537 (2012)
33. Spiller P J et al., in *Proc. of the 5th Intern. Particle Accelerator Conf., IPAC'14, June 15–20, 2014, Dresden, Germany* (Eds C Petit-Jean-Genaz et al.) (Geneva: JACoW Publ., 2014) p. 1857
34. Tuzikov A et al., in *Proc. of the 25th Russian Particle Accelerator Conf., RuPAC'2016, St. Petersburg, Russia, November 21–25, 2016* (Geneva: JACoW Publ., 2016) p. 160
35. Syresin E M *Phys. Part. Nucl. Lett.* **12** 591 (2015); *Pis'ma Fiz. Elem. Chast. At. Yad.* **12** 916 (2015)
36. Kudashkin A et al., in *Proc. of the 25th Russian Particle Accelerator Conf., RuPAC'2016, St. Petersburg, Russia, November 21–25, 2016* (Geneva: JACoW Publ., 2016) p. 83
37. Chaize J-M et al., in *Proc. of the 7th Biennial Intern. Conf. on Accelerator and Large Experimental Physics Control Systems, ICALEPCS'99, 4–8 October 1999, Trieste, Italy* (Eds D Bulfone, A Daneels) (Trieste: Elettra, 2001) p. 475
38. Averichev A S et al. "Itogi 46-go i 47-go Seansov Nuklotrona" ("Results of 46th and 47th Nuclotron runs"), Rapid Communications JINR 9-2013-140 (Dubna: JINR, 2013)
39. Gorbachev E V et al. *Phys. Part. Nucl. Lett.* **13** 573 (2016); *Pis'ma Fiz. Elem. Chast. At. Yad.* **13** 905 (2016)
40. Ceph, https://ceph.io
41. Sedykh G S, Gorbachev E V, Elkin V G *Phys. Part. Nucl. Lett.* **17** 669 (2020); *Pis'ma Fiz. Elem. Chast. At. Yad.* **17** 615 (2020)
42. Butenko A V et al., in *Proc. of the 27th Linear Accelerator Conf., LINAC 2014, 31 August – 5 September 2014, Geneva, Switzerland* (Geneva: JACoW, 2014) p. 1068
43. Bazanov A M et al., in *Proc. of the 8th Intern. Particle Accelerator Conf., IPAC2017, 14–19 May, 2017, Copenhagen, Denmark* (Geneva: JACoW, 2017) p. 2362
44. Butenko A et al., in *Proc. of the 12th Intern. Particle Accelerator Conf. IPAC, 24–28 May 2021, Campinas, Brazil* (Eds L Lin et al.) (Geneva: JACoW Publ., 2021) p. 123
45. Bazanov A M et al. *Phys. Scr.* **95** 055307 (2020)
46. Hancock S, Knaus P, Lindroos M, in *Proc. of the 6th European Particle Accelerator Conf., EPAC'1998, 22–26 June 1998, Stockholm, Shweden* (Eds S Myers et al.) (Stockholm, 1998) p. 1520
47. Zhabitsky V M *Phys. Part. Nucl. Lett.* **15** 767 (2018); *Pis'ma Fiz. Elem. Chast. At. Yad.* **15** 694 (2018)
48. Ruckelt T, Alhumaidi M, Zoubir A M, in *Proc. of the 2nd Intern. Beam Instrumentation Conf., IBIC 2013, September 16–19, 2013, Oxford, UK* (Didcot: Diamond Light Source, 2013) p. 128
49. Butenko A V et al. *JETP Lett.* **113** 752 (2021); *Pis'ma Zh. Eksp. Teor. Fiz.* **113** 784 (2021)
50. Butenko A et al., in *Proc. of the 27th Russian Particle Accelerator Conf., RuPAC 2021, 27 September – 1 October 2021, Alushta, Russia* (Eds M Kuzin, V R W Schaa) (Geneva: JACoW, 2021) p. 7, https://doi.org/10.18429/JACoW-RuPAC2021-MOY01
51. Donets E D et al. *EPJ Web Conf.* **177** (5) 08002 (2018)
52. Syresin E et al., in *Proc. of the 13th Intern. Particle Accelerator Conf., IPAC2022, 12–17 June 2022, Bangkok, Thailand* (Eds F Zimmermann et al.) (Geneva: JACoW Publ., 2022) p. 1819, https://doi.org/10.18429/JACoW-IPAC2022-WEPOPT001